

# Towards a critical endpoint in the valence fluctuating $\text{Eu}(\text{Rh}_{1-x}\text{Co}_x)_2\text{Si}_2$ system

Franziska Walther,<sup>1,\*</sup> Michelle Ocker,<sup>1</sup> Alexej Kraiker,<sup>1</sup> Nubia Caroca-Canales,<sup>2</sup>  
Silvia Seiro,<sup>2,3</sup> Kristin Kliemt,<sup>1,†</sup> and Cornelius Krellner<sup>1</sup>

<sup>1</sup>*Kristall- und Materiallabor, Physikalisches Institut, Goethe-Universität Frankfurt,  
Max-von-Laue Stasse 1, 60438 Frankfurt am Main, Germany*

<sup>2</sup>*Max Planck Institute for Chemical Physics of Solids, 01187 Dresden, Germany*

<sup>3</sup>*Leibniz Institute for Solid State and Materials Research Dresden, 01069 Dresden, Germany*

(Dated: May 5, 2025)

We report on the successful single crystal growth of pure  $\text{EuRh}_2\text{Si}_2$  and of  $\text{Eu}(\text{Rh}_{1-x}\text{Co}_x)_2\text{Si}_2$  with  $x \leq 0.23$  by the flux method. Through Co substitution,  $\text{EuRh}_2\text{Si}_2$  can be tuned from stable antiferromagnetism via a valence-transition state towards the valence-crossover regime. From magnetization measurements, we constructed a  $B - T$  phase diagram for  $\text{EuRh}_2\text{Si}_2$  comprising multiple magnetic phases and showing a sizable magnetic anisotropy within the basal plane of the tetragonal unit cell. This indicates a complex antiferromagnetic ground state for  $x = 0$ . By applying positive chemical pressure through the substitution series  $\text{Eu}(\text{Rh}_{1-x}\text{Co}_x)_2\text{Si}_2$ , a sharp temperature-induced first-order phase transition is observed in magnetization, resistivity and heat capacity for  $0.081 \leq x \leq 0.119$ . The critical end point of this valence transition is located in the phase diagram in the vicinity of  $0.119 < x_{\text{EDX}} < 0.166$ . At higher substitution level, the system reaches a valence-crossover regime. The obtained results are presented in a temperature-substitution phase diagram.

## I. INTRODUCTION

In ternary europium-based intermetallic compounds a variety of intriguing electronic properties have been observed e.g. skyrmions [1, 2], nontrivial topological phases [3], colossal magnetoresistance [4–6] and in particular valence instabilities [7–9]. While these intriguing phenomena originate from electronic ordering, recent years have seen a growing focus on harnessing the emergence of novel effects resulting from the strong coupling between electronic and lattice degrees of freedom. An exemplary material that shows the emergence of a new form of elasticity due to electron-lattice coupling is the organic charge transfer salt  $\kappa\text{-(BEDT-TTF)}_2\text{Cu}[\text{N}(\text{CN})_2]\text{Cl}$ , which reveals a pressure-induced first-order Mott-metal-insulator transition, which terminates at a critical end point (CEP) [10]. By probing the elastic response of the material as it passes through the CEP, critical elasticity emerges around the CEP, characterized as the breakdown of Hooke's law. In order to study the electron-lattice coupling in intermetallic systems close to a CEP,  $4f$ -systems such as  $\text{YbInCu}_4$  [11] and  $\text{Eu}(\text{Pd}_2\text{Si}_{1-x}\text{Ge}_x)_2$  [12, 13] have proven to be suitable systems, as they show first-order valence transitions accompanied by pronounced changes in the crystal lattice.

In Eu compounds crystallizing in the  $\text{ThCr}_2\text{Si}_2$ -type structure, the Eu ions can adopt a magnetic divalent state, which is associated with a large unit cell volume, as observed in the antiferromagnetic compound  $\text{EuRh}_2\text{Si}_2$  [14]. Alternatively, Eu can exist in a non-magnetic trivalent state with a smaller unit cell, as in  $\text{EuCo}_2\text{Si}_2$ , where only Van Vleck paramagnetism is

present [15]. This is because the valence configurations of  $\text{Eu}^{2+}$  and  $\text{Eu}^{3+}$  are energetically rather close [16] and thus intermediate-valence states between a nearly divalent  $\text{Eu}^{(2+\delta)+}$ , ( $\delta < 1$ ), and a nearly trivalent electronic state  $\text{Eu}^{(3-\delta') +}$ , ( $\delta' < 1$ ) may emerge. These valence fluctuations can be driven by different external parameters such as temperature [17], pressure [7, 18], magnetic field [19] and substitution [20, 21]. The general  $p$ - $T$  phase diagram for Eu compounds, crystallizing in the  $\text{ThCr}_2\text{Si}_2$  type structure, reveals a stable divalent electronic state of Eu at low pressures (i.e. large unit-cell volume) and low temperatures with magnetic ordering. With increasing pressure, the magnetic ordering disappears abruptly and the systems show a valence transition from  $\text{Eu}^{2+}$  to  $\text{Eu}^{(3-\delta') +}$  with temperature [22]. These first-order phase transitions terminate in a critical end point (CEP) of second order, while the system enters a valence-crossover regime beyond the CEP at high pressures (small unit-cell volume). In proximity of the critical end point, the magneto-elastic coupling of the valence transition may lead to the occurrence of critical elasticity as observed in [10].

In order to study the electron-lattice coupling close to the critical end point using external pressure, a material system which is localized at the low-pressure side of the CEP has to be found. By applying hydrostatic pressure, it is then possible to pass through the region of putative critical elasticity and probe the elastic response of the system. A suitable material that can be tuned by chemical pressure in the vicinity of the CEP is  $\text{EuRh}_2\text{Si}_2$ . Previous studies under hydrostatic pressure [23] show a stable divalent state at pressures  $p \leq 0.96$  GPa and a valence transition realized between  $0.96 \leq p \leq 2$  GPa, which terminates at an estimated pressure of  $p_{\text{CEP}} = 2.05$  GPa at the critical end point.

To induce positive chemical pressure comparable to hydrostatic pressure, an isoelectronic and isostructural sub-

\* [franziska.walther@stud.uni-frankfurt.de](mailto:franziska.walther@stud.uni-frankfurt.de)

† Corresponding author: [kliemt@physik.uni-frankfurt.de](mailto:kliemt@physik.uni-frankfurt.de)

stitution is required, e.g. substitution of Rh atoms by smaller Co atoms in the series  $\text{Eu}(\text{Rh}_{1-x}\text{Co}_x)_2\text{Si}_2$ . Since  $\text{EuCo}_2\text{Si}_2$  crystallizes in the same structure with a 11% smaller unit cell [24], a large compression of the unit cell is expected, when Co is introduced into the lattice. Under the assumption of a linear decrease of the lattice parameters with  $x$  and correspondingly a linear decrease of the unit-cell volume (Vegards law), the hydrostatic pressure can be calculated using a typical bulk modulus of  $\text{EuRh}_2\text{Si}_2$  of  $K = 100 \text{ GPa}$  [22]. Hence, the valence transition should take place for substitution levels between  $0.08 \leq x \leq 0.18$  while the CEP is expected for  $x^{\text{CEP}} = 0.18$ . Compared to another substitution series  $\text{Eu}(\text{Rh}_{1-x}\text{Ir}_x)_2\text{Si}_2$  [25], where the CEP is localized in the range of  $0.5 < x < 0.75$ , in the here presented system a lower substitution level is necessary to reach the CEP. This is important, as higher substitution concentrations can induce more disorder in the system, and thus strongly affect the behavior at the CEP. So far, the substitution series with Co has been investigated on polycrystalline samples for  $x = 0.4$  by high-energy resolution fluorescence detection X-ray absorption spectroscopy (HERFD-XAS) [26] and hard x-ray photoemission spectroscopy [27] as well as for  $x = 0.1, 0.2, 0.3$  by x-ray absorption spectroscopy (XAS) [27]. In contrast to the pure system  $\text{EuRh}_2\text{Si}_2$ , which shows a temperature-independent Eu valence of  $\sim 2.1$  [27] for  $x = 0.4$  a gradual increase of the Eu valence from 2.57 at 300 K to 2.92 K is observed [27] indicating the valence crossover. For lower substitution concentrations with  $x = 0.1$ , a drastic valence change occurs from 2.2 at 300 K to 2.5 at 18 K, characteristic for a valence transition [27]. Hence, the substitution series  $\text{Eu}(\text{Rh}_{1-x}\text{Co}_x)_2\text{Si}_2$  is a promising system for studying valence fluctuations on single crystals, which couples to the crystal lattice.

In this work, single crystals of the pure system  $\text{EuRh}_2\text{Si}_2$  have been studied at first to examine their magnetic ground state by magnetization measurements with focus on the magnetic anisotropy within the basal plane of the crystal lattice. Chemical substitution may also affect magnetic anisotropy, as observed in  $\text{EuPd}_2(\text{Si}_{1-x}\text{Ge}_x)_2$  [12] and thus a detailed understanding of the complex anisotropic magnetic behavior is required. Then, the growth of single crystals of the substituted system  $\text{Eu}(\text{Rh}_{1-x}\text{Co}_x)_2\text{Si}_2$  for different substitution levels is reported, which will be characterized by measurements of magnetization, heat capacity, and resistivity.

## II. EXPERIMENTAL DETAILS

### A. Crystal Growth

The single crystal growth of  $\text{EuRh}_2\text{Si}_2$  as well as  $\text{Eu}(\text{Rh}_{1-x}\text{Co}_x)_2\text{Si}_2$  proved challenging due to a high melting point of rhodium with  $T_m = 1966^\circ\text{C}$ , which is combined with a low boiling point of europium with  $T_b = 1439^\circ\text{C}$  and therefore a high vapor pressure above

$1300^\circ\text{C}$ . To reduce the high melting point of rhodium, the flux method is used. Single crystals of  $\text{EuRh}_2\text{Si}_2$  were grown in indium flux using the Bridgman technique as described in [14]. Whereas single crystals of  $\text{Eu}(\text{Rh}_{1-x}\text{Co}_x)_2\text{Si}_2$  were grown in Eu-flux for different nominal substitution levels  $0.10 \leq x \leq 0.30$  with two initial compositions 1.8:2:2 and 2.5:2:2 as summarized in table I. On the first growth approaches, an additional prereaction of  $\text{Rh}_{1-x}\text{Co}_x$  was performed in an argon arc furnace (see Tab. I). High-purity starting materials Eu (EvoChem, 99.99%, pieces), Rh (EvoChem, 99.9%, powder; 99.9%, pieces), Co (Chempur, 99.99%, powder; Johnson Matthey Chemicals Limited, 99.9%, rod), Si (Cerac, 99.9999%, pieces) were placed in a screwable inner graphite crucible to avoid europium evaporation and to prevent a reaction of the highly reactive melt with the outer crucible material.

Depending on the initial mass of the melt ( $m = 2 \text{ g}$  and  $m = 4 \text{ g}$ ), graphite crucibles with different dimensions were used. The smaller graphite crucible has an inner diameter of  $\varnothing_i = 8 \text{ mm}$  and a length of  $l = 53 \text{ mm}$ , whereas the larger graphite crucible has a diameter of  $\varnothing_i = 13 \text{ mm}$  and a length  $l = 48 \text{ mm}$  (see Tab. I). The inner crucible is sealed in a niobium or tantalum outer crucible. The growth was carried out in a vertical resistive furnace (GERO HTRV70-250/18) under an argon atmosphere. The crucible was heated to  $1520^\circ\text{C}$ , homogenized for 5 hours, followed by a slow cooling period to  $1000^\circ\text{C}$  with  $4 \text{ K/h}$ . Finally, the furnace was cooled to room temperature with fast rate of  $150 \text{ K/h}$ .

TABLE I. Overview of single crystalline samples with nominal Co-concentration  $x_{\text{nom}}$ , incorporated Co-concentration  $x_{\text{EDX}}$  in the crystal determined by EDX-measurements, crucible size, stoichiometry and prereaction.

$x_{\text{EDX}}$	0.06	0.08	0.11	0.12	0.23
$x_{\text{nom}}$	0.10	0.3	0.2	0.2	0.3
crucible	small	large	large	small	small
initial composition $\text{Eu}:\text{Rh}_{1-x}\text{Co}_x:\text{Si}$	1.8:2:2	2.5:2:2	2.5:2:2	2.5:2:2	2.5:2:2
prereaction $\text{Rh}_{1-x}\text{Co}_x:\text{Si}$	✓	-	-	✓	-

For structural characterization, powder X-ray diffraction (PXRD) was performed using a Bruker D8 diffractometer ( $\text{Cu-K}\alpha$  radiation with  $\lambda = 1.5406 \text{ \AA}$  and Bragg-Brentano geometry). The chemical composition of the grown crystals, especially the substitution concentration  $x_{\text{EDX}} = \text{Co}/(\text{Rh}+\text{Co})$  was analyzed by energy-dispersive x-ray spectroscopy (EDX) using a Zeiss-DSM 940A scanning electron microscope with an EDAX detector. To determine the orientation of the grown single crystals and their crystallinity, a Müller Micro Laue instrument was used with white X-rays from a tungsten anode. The commercial Quantum Design Physical Property Measurement System (PPMS) was utilized to measure magnetization, heat capacity, and resistivity. The latter was determined using the four-point alternating current transport (ACT)

configuration. The heat capacity was measured with the thermal relaxation technique. A heating pulse is applied to the sample, afterwards the system slowly cools down and relaxes to thermal equilibrium. The heat capacity data was evaluated separately for the heating and cooling curves of a large heat pulse with a typical temperature rise of 30 K.

### III. RESULTS AND DISCUSSION

#### A. Structural and chemical characterization

The crystal growth yields small substituted single crystals with  $\leq 1$  mm in length (Fig. 1b). The evaluation of the Laue images shows that the thin plates are aligned in the  $a-a$  plane. The chemical composition of the 122 phase was confirmed by EDX measurements, which revealed two slightly different compositions with tiny variations in the contents of Eu and Si. Even within a single sample, regions deficient in Eu and enriched in Si can be observed. The stoichiometry ranges from  $\text{Eu}:(\text{Rh}+\text{Co}):\text{Si} = (16.9 \pm 0.30) : (39.9 \pm 1.2) : (43.1 \pm 1.1)$ , where the denoted uncertainties are the standard deviations of the average value, to a Eu-rich phase with a lower proportion of Si with  $\text{Eu}:(\text{Rh}+\text{Co}):\text{Si} = (19.7 \pm 1.60) : (41.2 \pm 0.4) : (39 \pm 1.6)$ . The latter phase is closer to the expected 1:2:2 stoichiometry. The  $(\text{Rh} + \text{Co})$  content is nearly constant in both phases. Furthermore, one has to mention that the Co concentration  $x_{\text{EDX}}$  in the crystal determined by EDX analysis is influenced by the Eu content, as in the EDX spectrum the Co-K line at  $E = 6.915$  keV overlaps with the Eu- $L_{\gamma_1}$  line at  $E = 6.891$  keV. Due to these measurement uncertainties, the amount of Co can be underestimated for low Co concentrations, when the Co peak is not very pronounced and lies on the shoulder of the Eu- $L_{\gamma_1}$  line.

In Tab. I, an overview of the growths performed for three different nominal substitution concentrations  $x_{\text{nom}} = 0.1; 0.2; 0.3$  is given, where  $x_{\text{EDX}}$  is the average Co concentration detected in the crystals within one batch by EDX measurement. Different concentrations  $x_{\text{EDX}}$  of Co were found in different batches with the same nominal concentration. Thus, the incorporation rate  $k_{\text{Co}} = x_{\text{nom}}/x_{\text{EDX}}$  depends on experimental parameters, such as the size of the crucible, mixing conditions, and whether or not a prereaction was performed. For a homogeneous incorporation of Co in the crystal, a sufficient mixing of the melt is necessary. Our results allow for the conclusion that a smaller crucible size allows for better mixing of the melt and leads to a higher incorporation of Co.

Powder x-ray diffraction confirmed the tetragonal structure with the  $I4/mmm$  space group for all substitution concentrations. In Fig. 1d, the diffractogram of  $\text{Eu}(\text{Rh}_{1-x}\text{Co}_x)_2\text{Si}_2$  for different substitution concentrations is shown for selected reflexes. No significant broadening of the reflexes was detected, suggesting that there was no large variation of the Co concentration within

the powder sample. For the high-intensity reflex (113) there is a shift to higher angles as the concentration  $x_{\text{EDX}}$  increases. This is due to the compression of the unit-cell volume, shown in Fig. 1c, as expected by applying positive chemical pressure. The volume of the unit cell decreases linearly with increasing substitution concentration for low concentrations, obeying Vegard's law, while a stronger decrease is observed for higher substitution levels  $x > 0.17$ . This results in a large relative unit cell compression of 4.8% for  $x_{\text{EDX}} = 0.23$ .

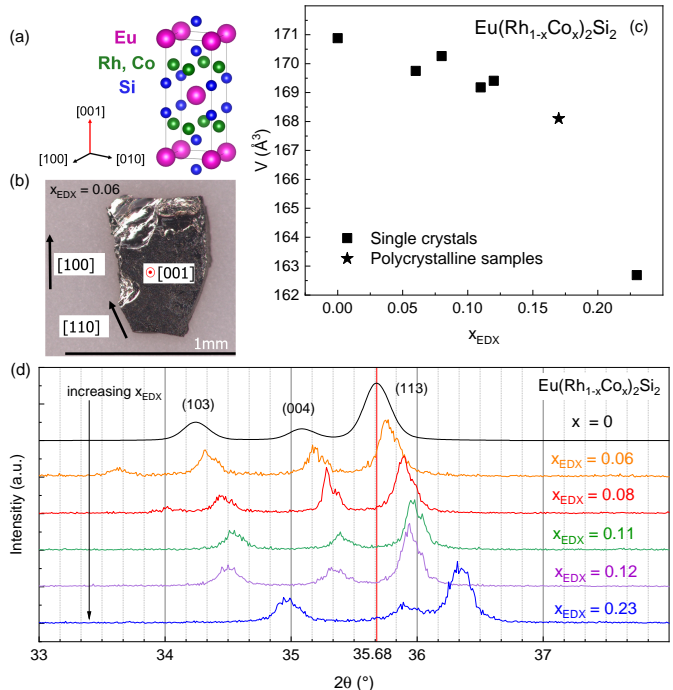


FIG. 1. (a):  $\text{ThCr}_2\text{Si}_2$ -type tetragonal crystal structure, (b): Single crystal with  $x_{\text{EDX}} = 0.06$ , (c): Unit-cell volume as function of Co concentration (d): X-ray diffractogram of the substitution series  $\text{Eu}(\text{Rh}_{1-x}\text{Co}_x)_2\text{Si}_2$  for selected reflexes. Black data for  $X = 0$  taken from [28].

#### B. $\text{EuRh}_2\text{Si}_2$

##### 1. Magnetization

In Fig. 2, the temperature-dependent magnetic susceptibility,  $\chi(T)$ , measured in zero field cooled (ZFC) and field cooled (FC) mode is compared for field aligned along the in-plane directions [100] and [110] for a small applied magnetic field of  $\mu_0 H = 0.005$  T. The compound  $\text{EuRh}_2\text{Si}_2$  undergoes three magnetic phase transitions below  $T_N = 24$  K. The transition temperatures at  $T_1$  and  $T_2$  were determined by the kink in the susceptibility of the ZFC curve, while  $T_1$  was taken as the midpoint of the rise. For the field applied along the [100] direction (black curve), the first transition appears at  $T_1 = 24.9$  K followed by the second transition at  $T_2 = 23.7$  K and a

possible first-order transition at  $T_3 = 11.6$  K as previously reported in reference [14] (open symbols in Fig. 2). Below  $T_3$ , the ZFC and FC curves differ, which may originate from a reorientation of magnetic domains or a ferromagnetic component. For field along the [110] direction (blue curve), only slight differences are observed for the transition temperatures with  $T_1 = 24.8$  K,  $T_2 = 23.4$  K and  $T_2 = 11.8$  K. However, the susceptibility at low temperatures for field along [100] is larger than for [110]. The observed negative susceptibility for the ZFC curve for field applied along the [110] direction is attributable to the diamagnetic signal of the quartz sample holder and a larger amount of GE varnish.

In the inset of Fig. 2 (a), the inverse magnetic susceptibility,  $\chi^{-1}(T)$ , for the field of  $\mu_0 H = 1$  T applied along the in-plane directions is shown, which exhibits Curie-Weiss behavior above  $T_N$ . Data were fitted using the Curie-Weiss expression in the temperature range  $150 \text{ K} \leq T \leq 300 \text{ K}$ . The obtained Curie-Weiss temperatures  $\Theta_{100} = (27 \pm 1) \text{ K}$  and  $\Theta_{110} = (29 \pm 1) \text{ K}$  as well as the effective magnetic moments  $\mu_{\text{eff}}^{100} = (7.7 \pm 0.1) \mu_B$  and  $\mu_{\text{eff}}^{110} = (7.8 \pm 0.1) \mu_B$  show no significant anisotropy between the in-plane directions as expected for a system with  $L = 0$  and negligible crystal electric field effects. The Curie-Weiss temperature for a field applied along the [100] direction is in accordance with [14]. The effective magnetic moment for both field directions is very close to the theoretically expected value for  $\text{Eu}^{2+}$  with  $\mu_{\text{eff}}^{\text{calc}} = 7.94 \mu_B$ .

In Fig. 2 (b), the magnetization as a function of the magnetic field,  $M(H)$ , at  $T = 2 \text{ K}$  is shown for the in-plane and out-of-plane directions. The data recorded with the field applied along the [001] direction reveal a continuous evolution with the magnetic field. However, a spin-flop-like transition with a sharp hysteresis appears below  $\mu_0 H = 1 \text{ T}$  for this field direction, where the origin is not clear yet. Since this pronounced hysteresis is reproducible in comparison to [14], we do not attribute the hysteresis to a misalignment of the sample. The data with field applied along an in-plane direction show metamagnetic transitions at  $B_1$ , accompanied by a hysteresis, Fig. 2(c), as already observed in [14] and the field-polarized state with  $7 \mu_B$  per Eu atom is reached at  $B_2$ . A clear in-plane anisotropy for the two field directions [100] and [110] is observed below  $B_2$ . The characteristic fields  $B_1$  and  $B_2$  were determined by the kink in the magnetization measured with increasing field.

In Fig. 2(d), the field-dependent magnetic susceptibility,  $M/\mu_0 H$  versus  $\mu_0 H$  is shown for different applied field directions to obtain information about the (re)orientation of magnetic moments for small magnetic fields, as demonstrated for the sister compound  $\text{GdRh}_2\text{Si}_2$  in [29]. There, a characteristic field dependence of the susceptibility was observed, which is indicative of a flipping of magnetic domains. In the case of  $\text{EuRh}_2\text{Si}_2$ , the situation is more complex but the low-field data is reminiscent of the  $\text{GdRh}_2\text{Si}_2$  case. The data show that a change in  $M/\mu_0 H$  occurs below  $B^{100,*} = 0.015 \text{ T}$

and below  $B^{110,*} = 0.007 \text{ T}$  which could be connected to a flipping of (a part of the) magnetic domains in the  $a-a$  plane. Even a small field is enough to reorient the magnetic moments out of the magnetic ground state configuration. Thus, the ground state and the spin configurations above  $B^*$  are energetically very close. Here, a weak magnetic in-plane anisotropy is observable. For the field applied along the [001] direction (red curve in Fig. 2(d)), the field-dependent magnetic susceptibility shows a constant behavior for low magnetic fields and suggests a nearly linear evolution of the magnetization with field. For a simple antiferromagnetic system, this corresponds to the case when the magnetic field is applied perpendicular to the magnetic sublattices. Thus, one suggests that the magnetic moments are aligned in the basal plane perpendicular to the [001] direction at very low fields. This is consistent with the proposed scenario of ferromagnetic layers stacked along  $c$  with a propagation vector  $(0, 0, \tau)$  [30] with moment alignment in the  $a-a$  plane observed through Mössbauer spectroscopy [31]. It is possible that the magnetic moments are slightly tilted out of the basal plane, which is not resolvable in the  $M/\mu_0 H$  representation. For instance, a small parallel component along the  $c$ -axis could thus generate a spin-flop-like transition as the one observed below  $\mu_0 H^{001} = 1 \text{ T}$  (red curve in Fig. 2(b)).

For field applied along the in-plane directions, we observe an abrupt increase at  $B_1$  which may be attributable to a reorientation of magnetic moments through a spin-flop-like transition. For the field applied along the [100] direction, this metamagnetic transition occurs at  $B_1 = 0.08 \text{ T}$ , Fig. 2(c), and the field-polarized state is reached at  $B_2 = 2.8 \text{ T}$ . However, for the [110] direction, a similar metamagnetic transition occurs in a magnetic field of  $B_1 = 0.07 \text{ T}$ . Above  $B_1$ , the magnetization increases smoother than in the case of a field applied along the [100] direction, and the field-polarized state is thus reached at a higher field of  $B_2 = 5.4 \text{ T}$ . The particular behavior shown in Fig. 2(c) reveals that the situation is complex as the spin-flop character occurs for both applied field directions. Furthermore, from the field dependence of the susceptibility,  $M(H)/H$ , of the inplane directions, one can deduce that the magnetic moments are arranged in a non-collinear structure in the basal plane, e.g. spiral or fan structure, which would be in line with the proposed incommensurable structure proposed in [14]. This hints at an alignment of the magnetic moments along a direction other than [100] or [110] for fields lower than  $B_1$  maybe in a further fan or spiral structure.

## 2. Phase diagram

From the magnetic susceptibility and magnetization data, Fig. 2 (data for higher fields and temperatures not shown), one can construct a field-temperature phase diagram for the [100] and [110] directions, which is shown in Fig. 3. The  $B-T$  phase diagram indicates four antiferro-



magnetic phases showing a complex magnetic structure. Below the Néel temperature  $T_N = 24$  K,  $\text{EuRh}_2\text{Si}_2$  enters the AFM 1 phase. With decreasing temperature, the AFM 2 phase appears at  $T_2$ , which slightly shifts to lower temperatures with increasing field. Further cooling forces a possible first-order transition at  $T_3$  into the low-temperature AFM 3 phase (fan / spiral structure with moments in plane). This phase stabilizes to higher temperatures with an increasing magnetic field. For small magnetic fields within the AFM 3 regime, the star symbol is assigned to the observed critical magnetic field  $B^*$  in the  $M/\mu_0 H$  versus  $\mu_0 H$  representation. We suspect another magnetic phase (with fan / spiral alignment of the moments in the  $a-a$  plane) at low temperatures and small fields below  $B^*$ , which represents the ground state of the material. However, the phase boundary lines are not yet clear. For magnetic fields larger than  $B_1$ , the system moves into the AFM 4 phase. At  $B_2$ , the field-polarized state is reached. In the phase diagrams, the weak in-plane anisotropy is reflected. For the [100] direction the AFM 4 is more stable for higher fields compared to the [110] direction, visible through the higher critical magnetic field  $B_2$  in the magnetization.

### C. $\text{Eu}(\text{Rh}_{1-x}\text{Co}_x)_2\text{Si}_2$

#### 1. Magnetization

Fig. 4 shows the magnetic susceptibility as a function of temperature for the cobalt concentration  $x_{\text{EDX}} = 0.07$  in comparison to  $x_{\text{EDX}} = 0$ , where the denoted substitution concentration was measured on the corresponding single crystal. The magnetic field was applied along the [100] direction. For the unsubstituted compound  $\text{EuRh}_2\text{Si}_2$  the magnetic transition at  $T_1$  occurs up to a critical magnetic field of  $\mu_0 H = 0.035$  T. For higher magnetic fields at 0.1 T, the transition is suppressed and merges in  $T_2$ . The substituted system with  $x_{\text{EDX}} = 0.07$  still reveals antiferromagnetic ordering, and the three magnetic transitions are observed at low fields. In contrast to  $x = 0$ , the transition at  $T_1$  is now visible up to a critical magnetic field of  $\mu_0 H = 0.1$  T, which leads to similar behavior of the 0.03 T curve of the unsubstituted system and the 0.1 T curve of the substituted sample with  $x_{\text{EDX}} = 0.07$ . While the transition temperature  $T_1$  remains constant under the influence of substitution, the AFM 1 phase is stabilized towards higher magnetic fields.

In Fig. 5(a), the temperature-dependent magnetic susceptibility of an  $x = 0.08$  sample is compared with samples of higher Co concentration of  $x_{\text{EDX}} > 0.07$ . The concentrations refer to the measured single crystals. For  $x_{\text{EDX}} = 0.08$  a steep increase in magnetic susceptibility with decreasing temperature is observed followed by a large drop. Between the cooling and the heating curve, a huge thermal hysteresis with a width of  $\sim 18$  K appears, which is characteristic for a first-order phase transition. These signatures are typical in Eu compounds for a va-

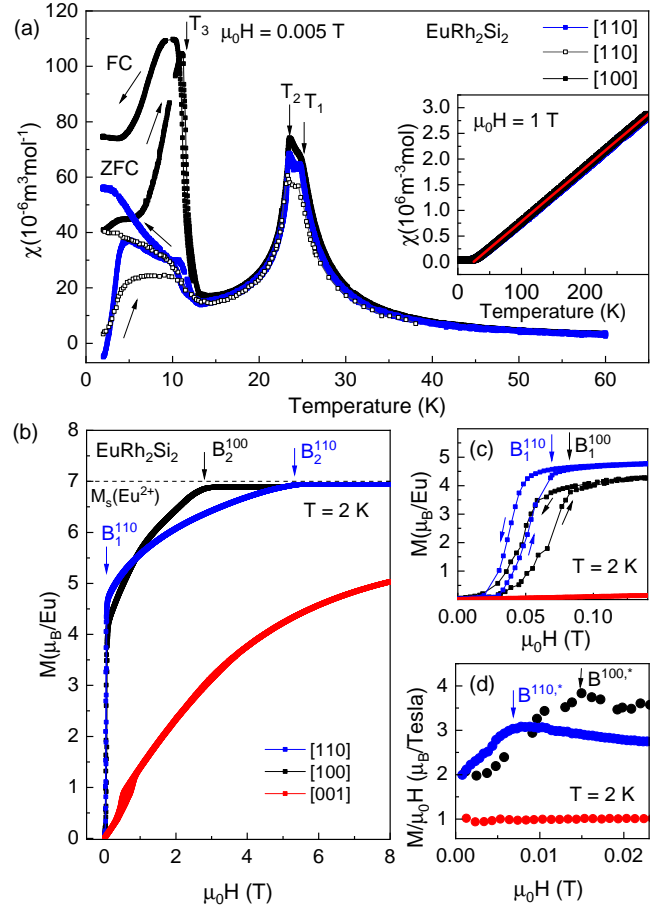


FIG. 2.  $\text{EuRh}_2\text{Si}_2$ : (a) Magnetic susceptibility as a function of temperature for field applied along the [100] and [110] directions at  $\mu_0 H = 0.005$  T. Data with open symbols are taken from [14]. Inset presents the temperature dependent inverse susceptibility at  $\mu_0 H = 1$  T for fields applied along the in-plane directions [100] and [110]. (b) Magnetization as a function of magnetic field for the in-plane and out-of-plane directions at  $T = 2$  K. (c) Spin-flop like transitions for the two in-plane directions at  $T = 2$  K. (d)  $M/\mu_0 H$  versus  $\mu_0 H$  for small magnetic field at  $T = 2$  K.

lence transition. The valence transition occurs at the valence transition temperature  $T_V = 44$  K, which is determined by the middle of the rise of the cooling curve. However, at  $T_N = 24$  K a small kink and thus antiferromagnetic ordering is still present. Possible origin may be a distribution of different Co concentrations within the sample, where a part of the sample with a lower concentration  $x_{\text{EDX}} \leq 0.07$  is still in the antiferromagnetically ordered regime. Another reason could be that not all Eu ions contribute to the valence transition, as suggested in Ref. [32], and thus some ions are still in the magnetically divalent state and give an antiferromagnetic contribution. With increased Co concentrations  $x_{\text{EDX}} = 0.116$  and  $x_{\text{EDX}} = 0.119$ , the valence transition is shifted to higher temperatures. The antiferromagnetic ordering is completely suppressed. The absence of magnetic ordering is

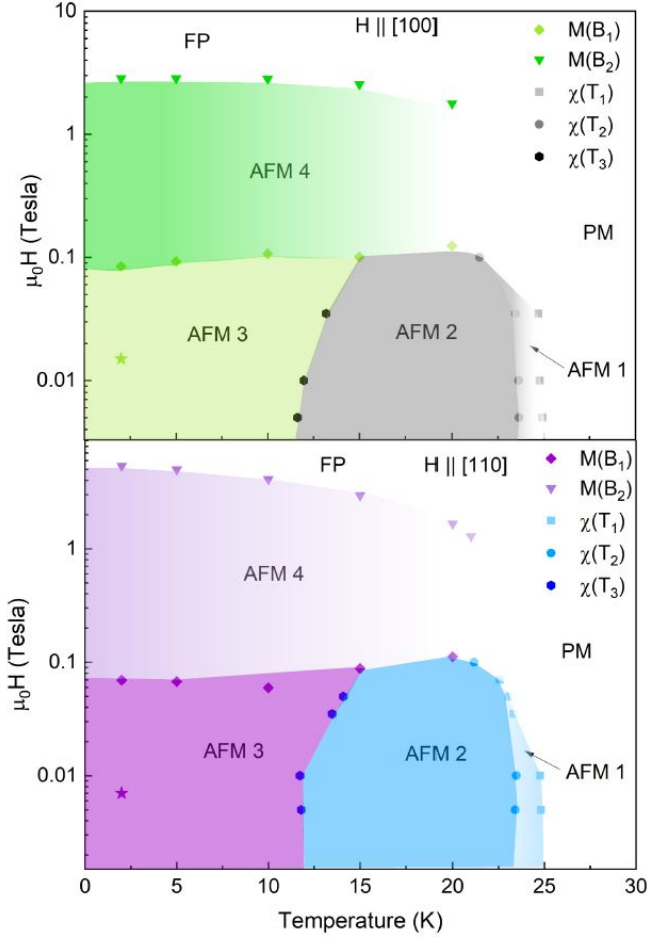


FIG. 3.  $\text{EuRh}_2\text{Si}_2$ : Magnetic phase diagram for field applied along [100] (top) and [110] (bottom).

also reflected in a reduced effective magnetic moment of  $\mu_{\text{eff}} = (5.8 \pm 0.4)\mu_B$  for  $x_{\text{EDX}} = 0.119$  compared with the large effective magnetic moment of  $\text{Eu}^{2+}$  for  $x = 0$  with  $\mu_{\text{eff}} = (7.76 \pm 0.08)\mu_B$ . The effective magnetic moment was obtained from a Curie-Weiss fit in the temperature range of 200 K to 300 K. For  $x_{\text{EDX}} = 0.116$  the valence transition occurs at  $T_V = 84$  K, and for  $x_{\text{EDX}} = 0.119$  at  $T_V = 105$  K. As expected from the general  $p$ - $T$  phase diagram following the first-order phase transition line, the hysteresis becomes smaller as the system gets closer to the valence crossover region. Between the  $x_{\text{EDX}} = 0.119$  and  $x_{\text{EDX}} = 0.116$  samples, slight changes in the Co substitution induce large differences in the valence transition temperature. Furthermore, tiny variations in the chemical composition can strongly affect the transition temperature as reported in [33] for the related compound  $\text{EuPd}_2\text{Si}_2$ . Since we observed the appearance of a homogeneity region for the 122 phase with minor differences in the Eu and Si concentrations, respectively, this could also cause the slight difference in  $T_V$ . With further increase of the substitution concentration, a moderate increase of the susceptibility at the valence crossover temperature

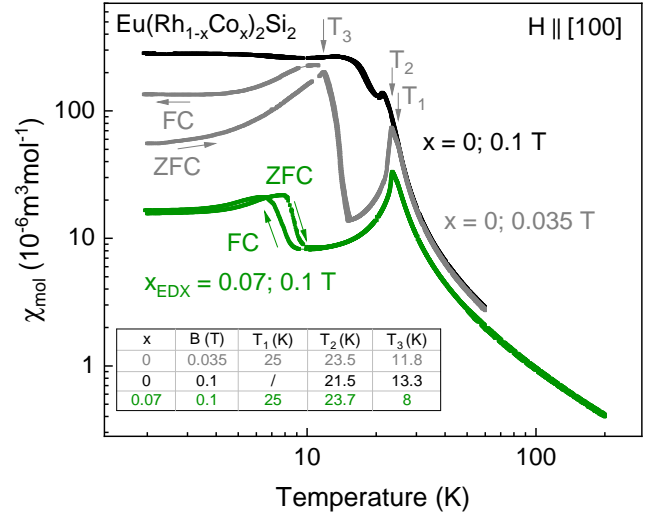


FIG. 4.  $\text{Eu}(\text{Rh}_{1-x}\text{Co}_x)_2\text{Si}_2$ : Magnetic susceptibility as a function of temperature for a sample with  $x = 0$  at  $\mu_0 H = 0.035$  T (grey curve) and  $\mu_0 H = 0.1$  T (black curve) as well as for a sample with  $x_{\text{EDX}} = 0.07$  at  $\mu_0 H = 0.1$  T (green curve). The magnetic field was applied along the [100] direction.

$T_V' = 220$  K for  $x_{\text{EDX}} = 0.228$  is observed, as shown in the inset of Fig. 5(a). In this case, there is no more thermal hysteresis. This suggests, that this concentration presents no first-order valence transition anymore but instead is situated in the valence-crossover regime.

## 2. Resistivity

To study the influence of Co substitution on the transport properties, temperature-dependent resistivity was measured for  $x_{\text{EDX}} = 0.126$  and  $x_{\text{EDX}} = 0.081$  (Fig. 5(b)). The resistivity was normalized to the value of the resistivity  $\rho(T = 300 \text{ K})$  of the cooling curve and the valence transition temperature was determined by the middle of the rise. For  $x_{\text{EDX}} = 0.126$  a sharp step appears at  $T_V = 95$  K with a large hysteresis of 15 K, which is characteristic of a first-order phase transition. The resistivity increases by one order of magnitude with temperature. During one cooling cycle, the sample undergoes the valence transition, which is associated with a large compression of the volume cell. This possibly leads to microcracks in the sample, and thus the resistivity in the following heating cycle is a factor of six higher compared to the cooling cycle, similar to what was observed in  $\text{Eu}(\text{Rh}_{1-x}\text{Ir}_x)_2\text{Si}_2$  [25]. For  $x_{\text{EDX}} = 0.081$  a sharp jump appears at  $T_V = 37$  K with a huge hysteresis of 23 K and an overall similar  $T$ -dependence as described before for the sample with  $x_{\text{EDX}} = 0.126$ . There is no anomaly of magnetic ordering at  $T_N = 25$  K as observed in the magnetic susceptibility.

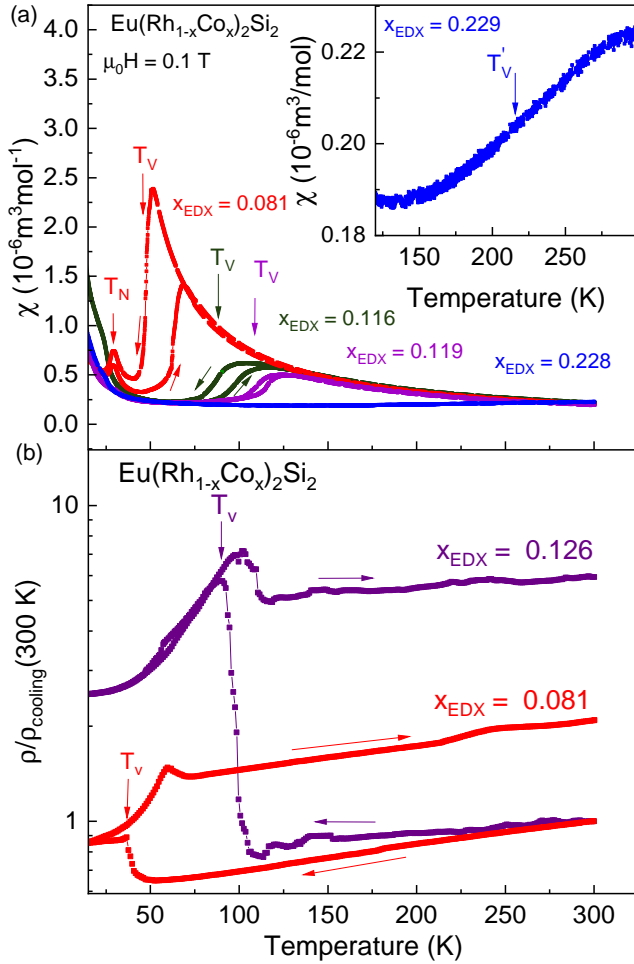


FIG. 5.  $\text{Eu}(\text{Rh}_{1-x}\text{Co}_x)_2\text{Si}_2$ : (a) Magnetic susceptibility as a function of temperature for three different Co concentrations at an applied magnetic field of  $B = 0.1$  T.  $T_V$  and  $T'_V$  denote the valence transition temperature and the valence crossover temperature, respectively. (b) Normalized temperature dependent electrical resistivity for two different Co concentrations.

### 3. Heat capacity

In Fig. 6(a), the heat capacity as a function of temperature is shown for a sample with  $x_{\text{EDX}} = 0.126$ . In accordance with the resistivity data displayed in Fig. 5(b), the heat capacity shows an anomaly at the valence transition temperature  $T_V = 95$  K. To investigate the first-order nature of the phase transition, the heat pulses were evaluated separately for the cooling (blue data) and heating (red data) process with single-slope analysis. A large difference of  $\sim 10$  K is observed between the valence transition temperature for the cooling curve,  $T_V^{\text{cooling}} = 96$  K and the heating curve,  $T_V^{\text{heating}} = 106$  K. The hysteresis that appears in the heat capacity is a further indication of a first-order phase transition and to the best of our knowledge has not yet been observed in heat-capacity

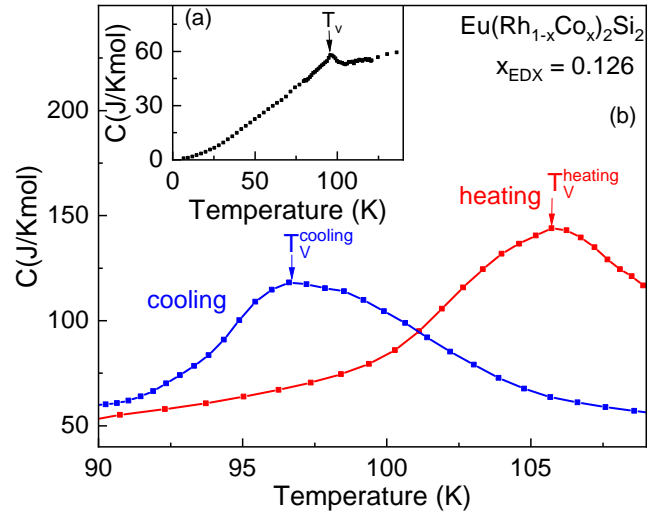


FIG. 6.  $\text{Eu}(\text{Rh}_{1-x}\text{Co}_x)_2\text{Si}_2$ : (a) Heat capacity as a function of temperature for  $x_{\text{EDX}} = 0.126$ . (b) Heat capacity as a function of temperature determined separately for cooling (blue curve) and heating (red curve) of long heat pulses through the valence transition.

measurements of Eu compounds showing a valence transition.

### 4. Phase diagram

We summarize our results obtained from the magnetic susceptibility and heat capacity measurements in a temperature-substitution phase diagram of  $\text{Eu}(\text{Rh}_{1-x}\text{Co}_x)_2\text{Si}_2$  with  $0.07 \leq x_{\text{EDX}} \leq 0.23$  in Fig. 7. For  $x_{\text{EDX}} \leq 0.07$ , europium is still in the divalent state and shows antiferromagnetic ordering below  $T_N = 24$  K. Although a clear increase of the magnetic ordering temperature is not observed for  $x_{\text{EDX}} = 0.07$ , as expected from the general Eu phase diagram [22] and pressure experiments on  $\text{EuRh}_2\text{Si}_2$  [23], an enhanced critical magnetic field of the AFM 1 phase is realized, which might indicate the stabilization of magnetic order. For increasing cobalt concentration, the system reveals a sharp valence transition for  $x_{\text{EDX}} = 0.081$ , which is expected to occur between the magnetic divalent  $\text{Eu}^{2+}$  and the valence-fluctuating  $\text{Eu}^{(3-\delta')\dagger}$  state. This first-order phase transition is characterized by a pronounced thermal hysteresis in the magnetic susceptibility, the resistivity, as well as in the heat capacity. A further increase of the substitution concentration within the valence transition regime from  $x_{\text{EDX}} = 0.081$  to  $x_{\text{EDX}} = 0.126$  results in an almost linear increase of the valence transition temperature towards higher temperatures. This is accompanied by a decrease in the width of the first-order hysteresis, and thus shows that the critical endpoint is approached. For the concentration level  $x_{\text{EDX}} = 0.166$ , the system enters the valence crossover regime with the interme-

diate  $\text{Eu}^{(2+\delta)+}$  state at high temperatures, which was observed in the heat-capacity data of a polycrystalline sample (not shown). Hence, the critical endpoint, where the first-order transition terminates followed by the crossover region can be localized in the region  $0.119 < x_{\text{EDX}}^{\text{CEP}} < 0.166$ . With further increasing concentration, the valence crossover transition was clearly observed in the susceptibility of a single crystal with  $x_{\text{EDX}} = 0.23$  at higher temperatures, where thermal hysteresis no longer occurs, indicating the crossover regime. In addition, this valence crossover takes place in a much broader temperature range of about 120 K. Further increasing of the cobalt concentration may shift the valence crossover transition to room temperature. Compared to the substitution series  $\text{Eu}(\text{Rh}_{1-x}\text{Ir}_x)_2\text{Si}_2$  [25], where the critical end point is located in the range of  $0.5 < x < 0.75$  and thus a strong influence of disorder is expected, in  $\text{Eu}(\text{Rh}_{1-x}\text{Co}_x)_2\text{Si}_2$  the critical endpoint can be approached with a lower substituent concentration level. This opens the possibility to study in detail the properties around the CEP, with lower amount of disorder.

The valence transition/crossover caused by chemical pressure can now be compared to hydrostatic pressure applied on  $\text{EuRh}_2\text{Si}_2$  single crystals [23]. The degree of substitution can be converted to pressure using the formula  $p_{\text{Co}} = \Delta V/V(x=0) \cdot K$ , where  $K$  denotes the bulk modulus. Here, a typical bulk modulus of  $K = 100 \text{ GPa}$  [22] is assumed.  $\Delta V/V$  indicates the change in unit cell volume with respect to unit-cell volume  $V$  for  $x = 0$  and can be taken from the PXRD data shown in Fig. 1(c). Thus, for chemical induced pressures below  $p_{\text{Co}} \leq 0.7 \text{ GPa}$  the system orders antiferromagnetically, which is comparable but slightly lower than reported in the work of Honda et al. [23], where the antiferromagnetic phase is stable up to  $p_{\text{AFM}} \leq 0.96 \text{ GPa}$ . For higher substitution levels, AFM ordering disappears and a first-order phase transition is realized between  $1.2 \leq p_{\text{Co}} \leq 1.7 \text{ GPa}$ . Comparing that to measurements under pressure, the valence transition occurs between  $0.96 \leq p \leq 2 \text{ GPa}$ . From substitution experiments, the critical endpoint would be estimated to be at  $p_{\text{Co}}^{\text{CEP}} = 1.7 \text{ GPa}$ , which is slightly lower in comparison to  $p^{\text{CEP}}$  evaluated in the hydrostatic pressure experiments [23]. The overall agreement between hydrostatic pressure experiments on pure  $\text{EuRh}_2\text{Si}_2$  crystals and the here presented substitution series  $\text{Eu}(\text{Rh}_{1-x}\text{Co}_x)_2\text{Si}_2$  is remarkable and shows, that the introduced disorder through cobalt substitution has only minor effects on the overall phase diagram.

#### IV. SUMMARY

In conclusion, we have succeeded in growing single crystals of the substitution series  $\text{Eu}(\text{Rh}_{1-x}\text{Co}_x)_2\text{Si}_2$  using Eu-flux. The chemical analysis revealed slight deviations from the ideal 1:2:2 stoichiometry with respect to Eu and

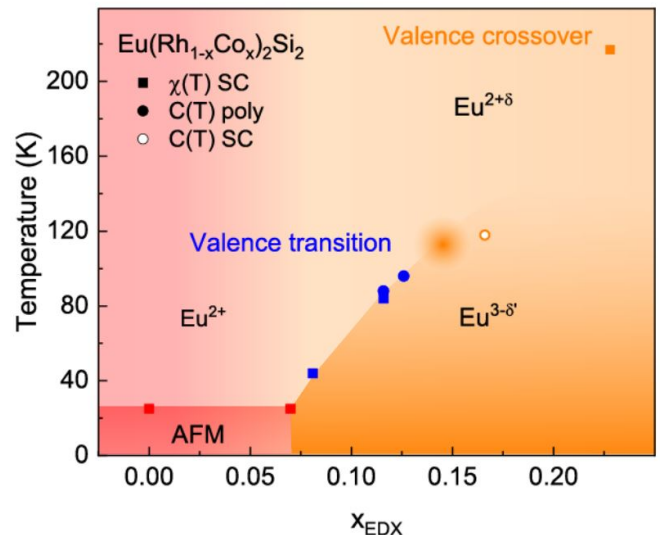


FIG. 7. Temperature - substitution phase diagram for  $\text{Eu}(\text{Rh}_{1-x}\text{Co}_x)_2\text{Si}_2$ .

Si, but with constant (Rh+Co) substitution level within a sample. For  $\text{EuRh}_2\text{Si}_2$ , we have found a weak magnetic anisotropy within the basal plane, which is reflected in different  $B - T$  phase diagrams for the [100] and [110] directions. These phase diagrams reveal a complex magnetic behavior and four different AFM phases could be clearly distinguished, while we suspect a fifth magnetic phase at low temperatures and small magnetic field representing the magnetic ground state. Based on these observations, for the substituted system with  $x_{\text{EDX}} = 0.07$  we observed an enhanced critical magnetic field of the AFM 1 phase, stabilized by the Co-substitution. Within the concentration range  $0.08 \leq x_{\text{EDX}} \leq 0.119$ , the system undergoes a first-order phase transition, where a valence transition from the magnetic divalent to the intermediate  $\text{Eu}^{(3-\delta') +}$  is realized, which is accompanied by the disappearance of the antiferromagnetic ordering. The first-order nature was revealed in magnetic susceptibility, resistivity, and heat capacity by a sharp and large hysteresis around the valence transition temperatures  $T_V$ . With increasing concentration level  $x_{\text{EDX}} \geq 0.15$ , the system changes to the valence crossover regime and no thermal hysteresis was observed at  $T_V' = 220 \text{ K}$ . As a result, we locate the critical endpoint in the vicinity of  $0.119 < x_{\text{EDX}} < 0.166$ . Therefore, the substitution level to approach the critical endpoint is rather low, which offers the possibility to study in detail the CEP under ambient or small hydrostatic pressures without sizeable amount of disorder. To this end, the presented substitution series  $\text{Eu}(\text{Rh}_{1-x}\text{Co}_x)_2\text{Si}_2$  is a suitable system to detect critical elasticity in an intermetallic compound.



## ACKNOWLEDGMENTS

We thank Christoph Geibel for valuable discussions and T. Förster for technical support. We acknowledge funding by the Wilhelm and Else Heraeus Foundation

and the Deutsche Forschungsgemeinschaft (DFG, German Research Foundation) via the TRR 288 (422213477, project A03).

## V. REFERENCES

- [1] M. Kakihana, D. Aoki, A. Nakamura, F. Honda, M. Nakashima, Y. Amako, T. Takeuchi, H. Harima, M. Hedo, T. Nakama, and Y. Ōnuki, Unique Magnetic Phases in the Skyrmion Lattice and Fermi Surface Properties in Cubic Chiral Antiferromagnet EuPtSi, *Journal of the Physical Society of Japan* **88**, 094705 (2019).
- [2] J. G. Sereni, I. Čurlík, M. Reiffers, and M. Giovannini, Evidence for magnetic dimers and skyrmion lattice formation in Eu<sub>2</sub>Pd<sub>2</sub>Sn, *Phys. Rev. B* **108**, 014427 (2023).
- [3] S. X. Riberolles, T. V. Trevisan, B. Kuthanazhi, T. Heitmann, F. Ye, D. Johnston, S. Bud'ko, D. Ryan, P. Canfield, A. A. V. Kreyssig, R. J. McQueeney, L. L. Wang, P. P. Orth, and B. G. Ueland, Magnetic crystalline-symmetry-protected axion electrodynamics and field-tunable unpinned Dirac cones in EuIn<sub>2</sub>As<sub>2</sub>, *Nature communications* **12**, 999 (2021).
- [4] S. Krebber, M. Kopp, C. Garg, K. Kummer, J. Sichelschmidt, S. Schulz, G. Poelchen, M. Mende, A. V. Virovets, K. Warawa, M. D. Thomson, A. V. Tarasov, D. Y. Usachov, D. V. Vyalikh, H. G. Roskos, J. Müller, C. Krellner, and K. Kliemt, Colossal magnetoresistance in EuZn<sub>2</sub>P<sub>2</sub> and its electronic and magnetic structure, *Phys. Rev. B* **108**, 045116 (2023).
- [5] J. C. Souza, S. M. Thomas, E. D. Bauer, J. D. Thompson, F. Ronning, P. G. Pagliuso, and P. F. S. Rosa, Microscopic probe of magnetic polarons in antiferromagnetic Eu<sub>5</sub>In<sub>2</sub>Sb<sub>6</sub>, *Phys. Rev. B* **105**, 035135 (2022).
- [6] R. S. Manna, P. Das, M. de Souza, F. Schnelle, M. Lang, J. Müller, S. von Molnár, and Z. Fisk, Lattice Strain Accompanying the Colossal Magnetoresistance Effect in EuB<sub>6</sub>, *Phys. Rev. Lett.* **113**, 067202 (2014).
- [7] G. Dionicio, H. Wilhelm, Z. Hossain, and C. Geibel, Temperature- and pressure-induced valence transition in EuCo<sub>2</sub>Ge<sub>2</sub>, *Physica B: Condensed Matter* **378-380**, 724 (2006), proceedings of the International Conference on Strongly Correlated Electron Systems.
- [8] A. Mitsuda, H. Wada, M. Shiga, and T. Tanaka, The Eu valence state and valence transition in Eu(Pd<sub>1-x</sub>Pt<sub>x</sub>)<sub>2</sub>Si<sub>2</sub>, *Journal of Physics: Condensed Matter* **12**, 5287 (2000).
- [9] C. U. Segre, M. Croft, J. A. Hodges, V. Murgai, L. C. Gupta, and R. D. Parks, Valence Instability in Eu(Pd<sub>1-x</sub>Au<sub>x</sub>)<sub>2</sub>Si<sub>2</sub>: The Global Phase Diagram, *Phys. Rev. Lett.* **49**, 1947 (1982).
- [10] E. Gati, M. Garst, R. S. Manna, U. Tutsch, B. Wolf, L. Bartosch, H. Schubert, T. Sasaki, J. A. Schlueter, and M. Lang, Breakdown of hooke's law of elasticity at the mott critical endpoint in an organic conductor, *Science Advances* **2**, e1601646 (2016).
- [11] M. Ocker, B. Ghebretinsae, J.-N. Zimmermann, S. Würtele, B. Wolf, A. Virovets, M. Lang, K. Kliemt, and C. Krellner, Single crystal growth and physical characterization to fine tune YbIn<sub>1-x</sub>T<sub>x</sub>Cu<sub>4</sub> (T = Au, Ag) towards the critical endpoint of the valence transition, [to be published \(2025\)](#), [arXiv:2501.17714 \[cond-mat.str-el\]](#).
- [12] M. Peters, K. Kliemt, M. Ocker, B. Wolf, P. Puphal, M. Le Tacon, M. Merz, M. Lang, and C. Krellner, From valence fluctuations to long-range magnetic order in EuPd<sub>2</sub>(Si<sub>1-x</sub>Ge<sub>x</sub>)<sub>2</sub> single crystals, *Phys. Rev. Mater.* **7**, 064405 (2023).
- [13] B. Wolf, T. Lundbeck, J. Zimmermann, M. Peters, K. Kliemt, C. Krellner, and M. Lang, Pressure study on the interplay between magnetic order and valence crossover in EuPd<sub>2</sub>(Si<sub>1-x</sub>Ge<sub>x</sub>)<sub>2</sub>, *Phys. Rev. B* **107**, 245147 (2023).
- [14] S. Seiro and C. Geibel, Complex and strongly anisotropic magnetism in the pure spin system EuRh<sub>2</sub>Si<sub>2</sub>, *Journal of Physics: Condensed Matter* **26**, 046002 (2013).
- [15] S. Seiro, K. Kummer, D. Vyalikh, N. Caroca-Canales, and C. Geibel, Anomalous susceptibility in single crystals of EuCo<sub>2</sub>Si<sub>2</sub> with trivalent Eu: Influence of excited J multiplets, *Physica Status Solidi (b)* **250**, 621 (2013).
- [16] A. Miedema, On the valence state of europium in alloys, *Journal of the Less Common Metals* **46**, 167 (1976).
- [17] K. Mimura, Y. Taguchi, S. Fukuda, A. Mitsuda, J. Sakurai, K. Ichikawa, and O. Aita, Bulk-sensitive high-resolution photoemission study of a temperature-induced valence transition system EuPd<sub>2</sub>Si<sub>2</sub>, *Journal of Electron Spectroscopy and Related Phenomena* **137-140**, 529 (2004).
- [18] F. Honda, K. Okauchi, A. Nakamura, D. Aoki, H. Akamine, Y. Ashitomi, M. Hedo, T. Nakama, and Y. Ōnuki, Pressure Evolution of Characteristic Electronic States in EuRh<sub>2</sub>Si<sub>2</sub> and EuNi<sub>2</sub>Ge<sub>2</sub>, *Journal of Physics: Conference Series* **807**, 022004 (2017).
- [19] A. Scherzberg, C. Sauer, U. Köbler, W. Zinn, and J. Röhler, Field induced valence shift in mixed valent EuCu<sub>2</sub>Si<sub>2</sub>, *Solid State Communications* **49**, 1027 (1984).
- [20] H. Wada, A. Nakamura, A. Mitsuda, M. Shiga, T. Tanaka, H. Mitamura, and T. Goto, Temperature- and field-induced valence transitions of EuNi<sub>2</sub>(Si<sub>1-x</sub>Ge<sub>x</sub>)<sub>2</sub>, *Journal of Physics: Condensed Matter* **9**, 7913 (1997).
- [21] S. Fukuda, Y. Nakanuma, J. Sakurai, A. Mitsuda, Y. Isikawa, F. Ishikawa, T. Goto, and T. Yamamoto, Application of Doniach Diagram on Valence Transition in EuCu<sub>2</sub>(Si<sub>x</sub>Ge<sub>1-x</sub>)<sub>2</sub>, *Journal of the Physical Society of Japan* **72**, 3189 (2003).
- [22] Y. Ōnuki, M. Hedo, and F. Honda, Unique Electronic States of Eu-based Compounds, *Journal of the Physical Society of Japan* **89**, 102001 (2020).
- [23] F. Honda, K. Okauchi, A. Nakamura, D. Li, D. Aoki, H. Akamine, Y. Ashitomi, M. Hedo, T. Nakama, and Y. Ōnuki, Pressure-Induced Valence Transition and Characteristic Electronic States in EuRh<sub>2</sub>Si<sub>2</sub>, *Journal of*

- the Physical Society of Japan **85**, 063701 (2016).
- [24] I. Mayer, J. Cohen, and I. Felner, X-ray and Moessbauer effect data of  $\text{EuM}_2\text{Si}_2$  compounds, *Acta Crystallographica, Section A: Crystal Physics, Diffraction, Theoretical and General Crystallography* **28**, 102 (1972).
  - [25] S. Seiro and C. Geibel, From stable divalent to valence-fluctuating behaviour in  $\text{Eu}(\text{Rh}_{1-x}\text{Ir}_x)_2\text{Si}_2$  single crystals, *Journal of Physics: Condensed Matter* **23**, 375601 (2011).
  - [26] Electronic Structure of the Valence Transition System  $\text{Eu}(\text{Rh}_{1-x}\text{T}_x)_2\text{Si}_2$  ( $\text{T} = \text{Co}, \text{Ir}$ ) Studied by High-Energy Resolution Fluorescence Detection X-Ray Absorption Spectroscopy, *Proceedings of the International Conference on Strongly Correlated Electron Systems (SCES2019)*.
  - [27] K. Ichiki, T. Matsumoto, H. Anzai, R. Takeshita, K. Abe, S. Ishihara, T. Uozumi, H. Sato, A. Rousuli, S. Ueda, Y. Taguchi, K. Shimada, H. Namatame, M. Taniguchi, S. Hamano, A. Mitsuda, H. Wada, and K. Mimura, Valence transition in polycrystalline  $\text{Eu}(\text{Rh}_{1-x}\text{Co}_x)_2\text{Si}_2$  studied by hard x-ray photoemission spectroscopy, *Journal of Electron Spectroscopy and Related Phenomena* **220**, 28 (2017).
  - [28] R. Ballestracci, *Comptes Rendus des Seances de l'Academie des Sciences, Serie B: Sciences Physiques*, 291 (1976).
  - [29] K. Kliemt, M. Hofmann-Kliemt, K. Kummer, F. Yakhov-Harris, C. Krellner, and C. Geibel,  $\text{GdRh}_2\text{Si}_2$ : An exemplary tetragonal system for antiferromagnetic order with weak in-plane anisotropy, *Phys. Rev. B* **95**, 134403 (2017).
  - [30] A. Chikina, M. Höppner, S. Seiro, K. Kummer, S. Danzenbächer, S. Patil, A. Generalov, M. Güttler, Y. Kucherenko, E. V. Chulkov, Y. M. Koroteev, K. Koepernik, C. Geibel, M. Shi, M. Radovic, C. Laubschat, and D. V. Vyalikh, Strong ferromagnetism at the surface of an antiferromagnet caused by buried magnetic moments, *Nature communications* **5**, 3171 (2014).
  - [31] I. Felner and I. Nowik, Itinerant and local magnetism, superconductivity and mixed valency phenomena in  $\text{RM}_2\text{Si}_2$ , ( $\text{R} = \text{rare earth}, \text{M} = \text{Rh}, \text{Ru}$ ), *Journal of Physics and Chemistry of Solids* **45**, 419 (1984).
  - [32] A. Mitsuda, H. Wada, R. Masuda, S. Kitao, M. Seto, Y. Yoda, and H. Kobayashi, Valence Transition of  $\text{EuRh}_2\text{Si}_2$  Studied by Synchrotron Mössbauer Spectroscopy, *Journal of the Physical Society of Japan* **89**, 104703 (2020).
  - [33] K. Kliemt, M. Peters, I. Reiser, M. Ocker, F. Walther, D.-M. Tran, E. Cho, M. Merz, A. A. Haghighirad, D. C. Hezel, F. Ritter, and C. Krellner, Influence of the Pd-Si Ratio on the Valence Transition in  $\text{EuPd}_2\text{Si}_2$  Single Crystals, *Crystal Growth & Design* **22**, 5399 (2022).